



# Climatology and annual cycle of global ocean dissolved oxygen represented by multiple observational gridded products

Juan Du<sup>1</sup>, Lijing Cheng<sup>2</sup>, Takamitsu Ito<sup>3</sup>, Hernan E. Garcia<sup>4</sup>, Zhankun Wang<sup>4</sup>, Jonathan D. Sharp<sup>5,6</sup>, Christopher J. Roach<sup>7</sup>, Shoshiro Minobe<sup>8</sup>, Yuntao Zhou<sup>9</sup>, Bin Lu<sup>10</sup>, Gian Giacomo Navarra<sup>11</sup>, and Seth M. Bushinsky<sup>12</sup>

<sup>1</sup>International Center for Climate and Environment Sciences, Institute of Atmospheric Physics, Chinese Academy of Sciences, Beijing, China

<sup>2</sup>State Key Laboratory of Earth System Numerical Modeling and Application, Institute of Atmospheric Physics, Chinese Academy of Sciences, Beijing, China

<sup>3</sup>School of Earth and Atmospheric Sciences, Georgia Institute of Technology, Atlanta, Georgia, USA

<sup>4</sup>NOAA, National Centers for Environmental Information, Silver Spring, Maryland, USA

<sup>5</sup>Cooperative Institute for Climate, Ocean, and Ecosystem Studies, University of Washington, Seattle, Washington, USA

<sup>6</sup>Pacific Marine Environmental Laboratory, National Oceanic and Atmospheric Administration, Seattle, Washington, USA

<sup>7</sup>Institute for Marine and Antarctic Studies, University of Tasmania, Hobart, Australia

<sup>8</sup>Department of Earth and Planetary Sciences, Faculty of Science, Hokkaido University, Sapporo, Japan

<sup>9</sup>School of Oceanography, Shanghai Jiao Tong University, Shanghai, China

<sup>10</sup>School of Information Science and Electronic Engineering, Shanghai Jiao Tong University, Shanghai, China

<sup>11</sup>Department of Geosciences, Princeton University, Princeton, New Jersey, USA

<sup>12</sup>Department of Oceanography, School of Ocean and Earth Science and Technology, University of Hawaii at Manoa, Honolulu, Hawaii, USA

**Correspondence:** Juan Du (dujuan10@mail.iap.ac.cn)

Received: 6 February 2026 – Discussion started: 13 February 2026

Revised: 28 April 2026 – Accepted: 30 April 2026 – Published: 11 May 2026

**Abstract.** Ocean dissolved oxygen ( $O_2$ ) is an essential climate variable crucial for sustaining the marine life; thus, changes of  $O_2$  at various spatiotemporal scales should be quantified and understood. Here, we study the climatology and annual cycle of  $O_2$  at regional to global scales using eight available gridded observational products. These datasets are generated by different groups using different primary data selection, quality control, bias correction, and interpolation methods, including statistical and machine-learning-based mapping methods. A common set of metrics was collaboratively developed by the community of the Gridded Observational Dataset Intercomparison Project-Dissolved Oxygen (GODIP-DO) to facilitate the inter-comparison. We find that global mean  $O_2$  profiles are consistent among all products ( $\pm 3 \mu\text{mol kg}^{-1}$ ), with the well-established decrease from high surface values to a minimum  $\sim 1000$  m, and subsequent increase to higher  $O_2$  at depth, although local differ-

ences could reach  $\pm 25 \mu\text{mol kg}^{-1}$  (0–1000 m). The hemispheric  $O_2$  annual cycle correlates strongly with ocean temperature changes, suggesting the key driver of temperature for the  $O_2$  annual cycle. However, there is substantial variation in the global mean 0–100 m  $O_2$  annual cycle, the magnitude ranges from  $-1$  to  $0.8 \mu\text{mol kg}^{-1}$ , with a standard deviation of the datasets of  $\sim 0.3 \mu\text{mol kg}^{-1}$ . Average oxygen minimum zones (OMZ) volume among the products is  $80.92 \times 10^6 \text{ km}^3$  ( $\pm 1.95\%$ ) for a  $60 \mu\text{mol kg}^{-1}$  threshold and  $152.00 \times 10^6 \text{ km}^3$  ( $\pm 1.72\%$ ) for a  $90 \mu\text{mol kg}^{-1}$  threshold. Our results help to depict and understand the spread among the available  $O_2$  gridded datasets.

## 1 Introduction

Anthropogenic climate change drives ocean warming, increases stratification, and alters ocean circulation (Bindoff et al., 2019). These changes lead to the loss of ocean dissolved oxygen ( $O_2$ ), namely deoxygenation, because of the changes in the  $O_2$  solubility, ventilation, and deep ocean respiration (Keeling et al., 2010; Schmidtko et al., 2017; Breitburg et al., 2018; Oschlies et al., 2017, 2018; Garcia-Soto et al., 2021). Deoxygenation occurred in most open ocean regions during the mid-20th to early 21st centuries, such as the Mediterranean Sea, tropical oxygen minimum zones (OMZ), and the North Atlantic Subtropical Gyre (Tan et al., 2026), influencing marine ecosystems through resulting biogeochemical feedbacks such as ocean productivity, nutrient cycling, carbon cycling, marine habitat, etc (Levin, 2018; Bindoff et al., 2019). Given its importance, studying  $O_2$  changes at various spatiotemporal scales becomes critical.

Observations and model simulations document a robust decline of the global  $O_2$  inventory, which is a grand challenge for the accurate assessment of deoxygenation (Ito et al., 2017; Schmidtko et al., 2017; Breitburg et al., 2018). For trends, current assessments such as the Intergovernmental Panel on Climate Change (IPCC) Special Report on the Ocean and Cryosphere in a Changing Climate (SROCC) indicates that the open ocean is losing  $O_2$  overall with a decadal variability of 0.3 %–2 % since the 1960s over all ocean depths and of 0.5 %–3.3 % between 1970 and 2010 from the ocean surface to 1000 m, with an expansion of OMZ by 3 %–8 % (Bindoff et al., 2019; Gulev et al., 2021; Zhou et al., 2022). In addition, a recent observational-based assessment by Tan et al. (2026) shows that significant signal emergence of long-term  $O_2$  trends (both deoxygenation and oxygenation) can now be detected across global ocean in a large-scale and deep-reaching pattern since the 1990s, although the regional data uncertainty still needs to be taken into account. These studies reveal substantial uncertainty in quantifying the open ocean  $O_2$  trends, however, there is no dedicated study assessing the available products on  $O_2$  climatology and its annual cycle, which is the key focus of the present study.

The differences among different  $O_2$  products may arise from the instruments/platforms used to obtain  $O_2$  profiles and the data processing techniques including quality control processes, bias correction approaches, vertical interpolation methods, mapping methods (horizontal interpolation), land-ocean masks, and so on. Since the late 19th century, oceanographers have measured ocean  $O_2$  using many observing systems with varying sampling resolutions. The very first observing system includes the chemical titration method developed by Winkler (Ocean Station Data, OSD), which restricted the  $O_2$  observations derived from water samples to several depth levels. Electrochemical and optical sensors for measuring  $O_2$  became prevalent in the 1960s–1970s and are now widely used to make continuous measurements on plat-

forms such as the CTD (Conductivity-Temperature-Depth) profilers. Biogeochemical Argo profiling floats (BGC-Argo) have provided increasing ocean  $O_2$  observation profiles since the early 2000s, and underwater gliders (GLD) and moorings are especially useful for regional oceanography (Grenouire et al., 2021; Gourteski et al., 2024b). The Winkler data are labour intensive with lower sampling resolution, whereas sensor-based measurements have better spatiotemporal resolution, and the proliferation of the BGC-Argo program has dramatically increased  $O_2$  observations.

With the ocean  $O_2$  observations collected using different observing systems, there have been several quality controlled global ocean  $O_2$  observation datasets from different research organizations/groups such as the National Centers for Environmental Information (NCEI) of the National Oceanic and Atmospheric Administration (NOAA) (Garcia et al., 2024; Garcia et al., 2018; Boyer et al., 2018), Shanghai Jiao Tong University (SJTU, Zhou et al., 2022) and the Institute of Atmospheric Physics (IAP) Chinese Academy of Sciences (Gourteski et al., 2024b). These quality controlled observations are then used to construct gridded  $O_2$  data products by filling data gaps with a mapping method where direct observations were not available. The available mapping methods include objective analysis (Garcia et al., 2024), ensemble optimal interpolation with dynamic ensemble (Cheng et al., 2024; Cheng et al., 2017; Cheng and Zhu, 2016), Data Interpolating Variational Analysis (DIVA; Roach and Bindoff, 2023), machine learning techniques (Sharp et al., 2023; Ito et al., 2024; Huang et al., 2023; Liu et al., 2025), and geostatistical regression (Zhou et al., 2022).

All the previously mentioned instrumental data have measurement errors and biases, and the data processing techniques are imperfect, leading to uncertainty in representing the  $O_2$  climatological mean state and its annual variation. A systematic multi-product intercomparison at regional to global scales could serve as the primary tool to assess the robustness of our observational understanding and to quantify the spread in current climatological representations. The spread among different datasets includes all uncertainty factors and is different from the recent single-factor assessment of Ito et al. (2025) who focused solely on mapping methods. In particular, we employed eight ocean  $O_2$  climatology products, covering statistical and machine-learning-based mapping methods whereas Ito et al. (2025) included statistical mapping methods only. Our analysis includes the gridded  $O_2$  dataset from IAP (Gourteski et al., 2024), World Ocean Atlas 2023 (hereafter, WOA23; Garcia et al., 2024) and World Ocean Atlas 2018 (hereafter, WOA18; Garcia et al., 2018; Boyer et al., 2018) by NCEI, a machine-learning-based data product by Sharp et al. (2023) (Gridded Ocean Biogeochemistry from Artificial Intelligence, hereafter, GOBAI; Sharp et al., 2023), two data products based on DIVA by Roach and Bindoff (2023) (hereafter, RB; Roach and Bindoff, 2023) and Global Ocean Data Analysis Project (hereafter, GLODAP; Lauvset et al., 2016), a geostatistical gridded  $O_2$  dataset from

SJTU (Zhou et al., 2022), and a machine-learning-based data product (hereafter, Jingwei; Lu et al., 2024).

The rest of the paper is organized as follows. The gridded datasets and methods employed in the study are presented in Sect. 2. In Sect. 3, the results of depicting the characteristics and assessing the spread of O<sub>2</sub> climatology and annual cycle for different products are introduced. The analysis related to OMZ distribution is also presented in Sect. 3. The results of the study are summarized and discussed in Sect. 4.

## 2 Datasets description

We used eight O<sub>2</sub> gridded products (IAP, WOA23, WOA18, GOBAI, RB, GLODAP, SJTU, and Jingwei) that are different in many aspects including the instruments to get raw O<sub>2</sub> profiles and also the data processing techniques, such as quality control and bias correction approaches, vertical interpolation methods, mapping methods, land-ocean masks, and so on (Table 1).

The observations used by IAP, WOA23, WOA18, RB, SJTU, and Jingwei are mainly from WOD (World Ocean Database, Boyer et al., 2018; Mishonov et al., 2024) and BGC-Argo. Observations from GLODAP are also used in GOBAI product. The IAP, WOA23, WOA18, and GOBAI datasets include monthly climatology, and the remaining four data products (RB, GLODAP, SJTU, and Jingwei) only provide the annual mean climatology. So, analyses related to the annual variation of the global ocean O<sub>2</sub> and the annual cycle are restricted to the four datasets with monthly climatology (IAP, WOA23, WOA18, and GOBAI). The gridded data products of IAP, WOA23, WOA18, RB, GLODAP, and Jingwei reach the ocean bottom of about 5500 m/6000 m. GOBAI and SJTU only cover the top 2000 m. The horizontal resolution of the data product of RB and SJTU is  $0.5^\circ \times 0.5^\circ$  and  $2^\circ \times 2^\circ$ , respectively, and all the other six products are at a resolution of  $1^\circ \times 1^\circ$ . The horizontal space coverages of all the datasets are also slightly different. The space coverage of the GOBAI data is limited by the distribution of the temperature and salinity data product on which it is based, so GOBAI only covers  $64.5^\circ\text{S}$ – $79.5^\circ\text{N}$  of the open ocean (O<sub>2</sub> in the coastal regions and oceans with complex topography are not reconstructed). The mapping method for WOA18 and WOA23 is based on objective analysis and that for IAP is the ensemble optimal interpolation with dynamic-ensemble. GLODAP and RB both adopt the DIVA method to generate gap-filled fields. SJTU develops the geostatistical regression interpolation method. The feed-forward neural network and the spatio-temporal graph hypernetwork are used for the machine learning process of the GOBAI and Jingwei data products, respectively (Table 1). To illustrate the spatiotemporal characteristics of the observation profiles, the spatial distribution and annual number of the three main observation platforms (OSD, CTD, BGC-Argo) for 1960–2024 are shown in Fig. 1.

This study used a common ocean mask, which is defined as ocean grid points with all data products available. The common land-ocean masks for the layers of 100 and 2000 m are presented in Fig. 2 and the common masks for the other layers (1000, 3000, 4000, and 5000 m) are available in Fig. S1 in the Supplement. This will be a uniform comparison and remove the impacts of different data coverage on the results. The datasets of RB and SJTU were interpolated to a common  $1^\circ \times 1^\circ$  resolution as all the other datasets to facilitate the comparison, but the interpolation has a negligible impact on the results presented in this work (less than 0.01 % for the global mean O<sub>2</sub>).

## 3 Results

### 3.1 Global mean O<sub>2</sub>

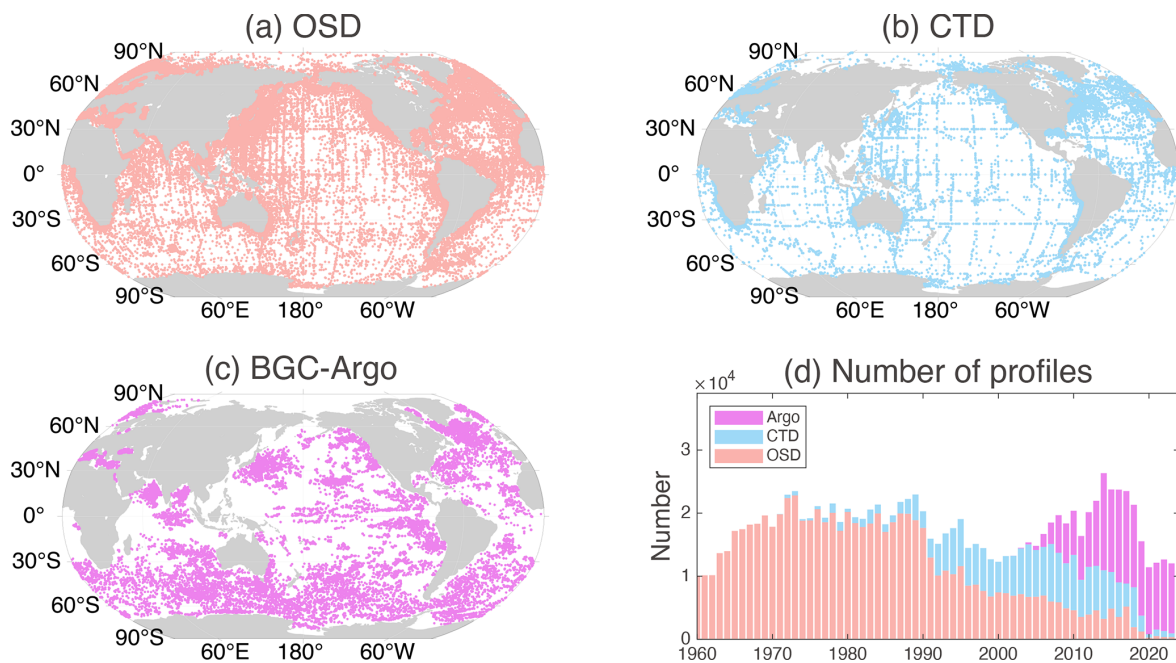
The global area-weighted mean O<sub>2</sub> profile is first presented in Fig. 3a, showing a well-established vertical structure and a good consistency among all products. O<sub>2</sub> is higher near the surface than in the deeper ocean because of the gas exchange with the atmosphere and photosynthesis. The O<sub>2</sub> reaches the lowest value at  $\sim 1000$  m because of the respiration and limited O<sub>2</sub> supply from the surface. The O<sub>2</sub> increases from  $\sim 1000$  m to the deep ocean ( $\sim 5000$  m) because of the weaker respiration and the intermediate, deep, and bottom water formation that supplies higher O<sub>2</sub> water into the deep layers, where cold, dense surface water sinks, and is then distributed globally by deep ocean currents, slowly losing O<sub>2</sub> along its centuries-long journey (Musun et al., 2023).

To better quantify the differences among the datasets, we take the difference between all seven other data products (WOA23, WOA18, GOBAI, RB, GLODAP, SJTU, and Jingwei), and IAP data (Fig. 3e–h). The differences are mostly within  $\pm 3 \mu\text{mol kg}^{-1}$  among all the datasets with a common land-ocean mask from ocean surface to 5500 m, except that the differences for SJTU and Jingwei range between  $-6$  and  $5 \mu\text{mol kg}^{-1}$  for the upper 200 m. The differences are comparable to the magnitude of O<sub>2</sub> anomaly, whose semi-decadal median is within  $\pm 10 \mu\text{mol kg}^{-1}$  within major ocean basins (Schmidt et al., 2017).

There is a negative offset between GOBAI and IAP ( $\sim -2 \mu\text{mol kg}^{-1}$ ). The differences between WOA18, RB, and IAP are positive. One possible reason for these differences is that different data products construct climatologies using data from different time periods with different resolutions. The SJTU climatology uses CTD, OSD, BGC-Argo, and additional GLD data, then interpolates them at coarser  $2^\circ \times 2^\circ$  resolution. The GOBAI climatology is reflective of a more recent period compared to the other datasets (2004–2024), which might at least partly explain the negative difference between GOBAI and IAP (where data from 1960–2022 are used). Because of the general deoxygenation trend, a “newer” climatology is expected to show less global mean

**Table 1.** Global ocean O<sub>2</sub> gridded datasets employed in the comprehensive inter-comparison of the climatology (EnOI-DE: ensemble optimal interpolation with dynamic-ensemble; OA: objective analysis; ML: machine learning; GR: geostatistical regression).

O <sub>2</sub> Datasets	Mapping	Quality Control	Time Period	Resolution	Depth/Layers	Observations
IAP Gourteski et al. (2024a)	EnOI-DE	IAP	1960–2022	1° × 1°	6000 m/119	OSD, CTD, BGC-Argo
WOA23 Garcia et al. (2024)	OA	NCEI	1965–2022	1° × 1°	5500 m/102	OSD, CTD, BGC-Argo
WOA18 Boyer et al. (2018)	OA	NCEI	1960–2017	1° × 1°	5500 m/102	OSD
GOBAI Sharp et al. (2023)	ML	GLODAP, BGC-Argo	2004–2024	1° × 1°	1975 m/58	OSD, BGC-Argo
RB Roach and Bind-off (2023)	DIVA	NCEI	1960–2017	0.5° × 0.5°	6100 m/108	OSD, CTD
GLODAPv2 Lauvset et al. (2016)	DIVA	GLODAP	1972–2013	1° × 1°	5500 m/33	OSD
SJTU Zhou et al. (2022)	GR	NCEI, SJTU	1960–2019	2° × 2°	2000 m/61	OSD, CTD, BGC-Argo, GLD
Jingwei Lu et al. (2024)	ML	NCEI	1960–2023	1° × 1°	5500 m/33	OSD, CTD, BGC-Argo

**Figure 1.** Spatial distribution ((a) OSD, (b) CTD, (c) BGC-Argo) and annual number (d) of observation profiles.

O<sub>2</sub> than an “older” climatology. IAP is close to WOA23 at the upper 2000 m within  $1 \mu\text{mol kg}^{-1}$ , which is reasonable because both IAP and WOA23 used bottle (OSD), CTD, and delayed-mode BGC-Argo data using the same  $1^\circ \times 1^\circ$  data resolution, and they have similar time coverage of data

used to generate climatology (IAP, 1960–2022, and WOA23, 1965–2022).

Below 2000 m, there is an offset between IAP and WOA23: WOA23 O<sub>2</sub> is  $0.2\text{--}0.6 \mu\text{mol kg}^{-1}$  higher than IAP. Possible explanations may be the differences in quality control and mapping methods. Another possibility is the “jump”

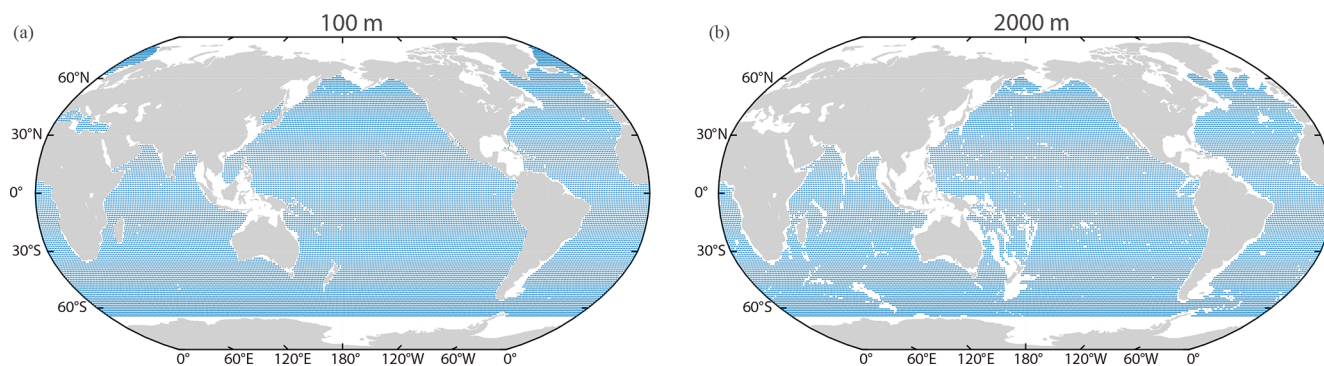


**Figure 2.** Grid point distribution of the common land-ocean mask for the layers of 100 m (a) and 2000 m (b).

around 2000 m of IAP minus WOA23. It is common to have a discontinuity around 2000 m because of the big differences in data amount and data distributions at upper and deeper layers (observations are concentrated in the upper ocean and most of the BGC-Argo data are in the upper 2000 m). Differences in infilling the empty grid nodes during the mapping procedure may also play a significant role in deep ocean layers where the number of observation data is severely limited. Results of applying different mapping methods to the same in situ datasets suggest that mapping methods may contribute to a difference of less than  $\pm 1 \mu\text{mol kg}^{-1}$  for the 0–5500 m area-weighted averaged  $\text{O}_2$  (Ito et al., 2025). And using two different quality control processes and the same mapping procedure yields a difference of only  $\pm 0.5 \mu\text{mol kg}^{-1}$  (Ito et al., 2025).

The mean  $\text{O}_2$  profiles and the differences between datasets for major ocean basins (Pacific, Atlantic, Indian) are calculated separately and presented in Fig. 3b–d and f–h. The differences are mostly within  $\pm 4 \mu\text{mol kg}^{-1}$  among all the datasets for the Pacific and Indian Oceans, except that the difference for Jingwei ranges between  $-8$  and  $2 \mu\text{mol kg}^{-1}$  for the upper 200 m in the Pacific Ocean (Fig. 3f). The mean  $\text{O}_2$  profiles for the Atlantic Ocean show more notable differences compared to other ocean basins (Fig. 3c), including that the mean  $\text{O}_2$  profile of SJTU data shows a difference of  $-10$  to  $-5 \mu\text{mol kg}^{-1}$  for the depth of 1000–2000 m, while the differences of all the other datasets are constrained to  $-5$  to  $5 \mu\text{mol kg}^{-1}$  from ocean surface to the depth of 5500 m (Fig. 3g). For the Atlantic Ocean, the mean  $\text{O}_2$  reached the minimum at the depth of  $\sim 500$  m (Fig. 3c), which is much shallower than the  $\text{O}_2$  minimum layers for the Pacific and Indian Oceans ( $\sim 1000$  m, Fig. 3b, d), possibly due to a combined effect of the formation, transport, and mixing process of the North Atlantic Deep Water (NADW), the ventilation processes such as Atlantic Meridional Ocean Circulation (AMOC), and so on (Levin, 2018; Koelling et al., 2022; Musan et al., 2023; Ruhl et al., 2025).

### 3.2 Zonal mean structure

The global zonal mean  $\text{O}_2$  concentration of the eight datasets for the upper 1000 m shows consistency for the zonal structure (Fig. 4a). There is a minimum of mean  $\text{O}_2$  levels around the tropical regions for all the datasets, associated with a shoaling of the tropical and subtropical thermocline depth (Deutsch et al., 2011) and the presence of the tropical upper ocean OMZ. The differences in the global zonal mean  $\text{O}_2$  for the upper 1000 m between the seven data products (WOA23, WOA18, GOBAI, RB, GLODAP, SJTU, and Jingwei) and IAP are shown in Fig. 4b. The differences in zonal mean 0–1000 m averaged  $\text{O}_2$  are mostly within  $\sim 5 \mu\text{mol kg}^{-1}$ . The zonal mean  $\text{O}_2$  difference between IAP and WOA23 is the smallest, which is generally within  $\sim 1.5 \mu\text{mol kg}^{-1}$ . The zonal mean of GOBAI is generally lower than that of IAP, especially in the Northern Hemisphere, which may imply stronger deoxygenation trends in the Northern Hemisphere, as the GOBAI climatology baseline is newer than that of IAP. The zonal mean of the RB dataset is higher than that of IAP by  $\sim 0.78 \mu\text{mol kg}^{-1}$  on average, consistent with the positive offset shown in Fig. 3. Jingwei dataset has the strongest differences from IAP and other products, showing a notable zonal fluctuation.

The results for the depth layers 0–600 and 0–2000 m (Fig. S2) show similar variation pattern to the depth layer 0–1000 m. The differences in the global zonal mean  $\text{O}_2$  between data products are mostly within  $\sim 5 \mu\text{mol kg}^{-1}$  for 0–600 m and within  $\sim 3 \mu\text{mol kg}^{-1}$  for 0–2000 m (Fig. S2b, d). For 0–600 m, the zonal mean  $\text{O}_2$  difference between IAP and WOA23 is the smallest and Jingwei shows the strongest differences from IAP and other products. For 0–2000 m, the depth average makes the difference between datasets much smaller. Jingwei still shows relatively large discrepancy from the other datasets in the regions around  $60^\circ\text{N}$  and the equator. Within the latitude range  $20^\circ\text{S}$  where all other data products show the best agreement, Jingwei exhibits a significant deviation of  $\sim 5 \mu\text{mol kg}^{-1}$  from the rest.

However, the zonal mean  $\text{O}_2$  concentration for 0–100 m (Fig. 4b) shows a relatively distinct pattern. The zonal mean

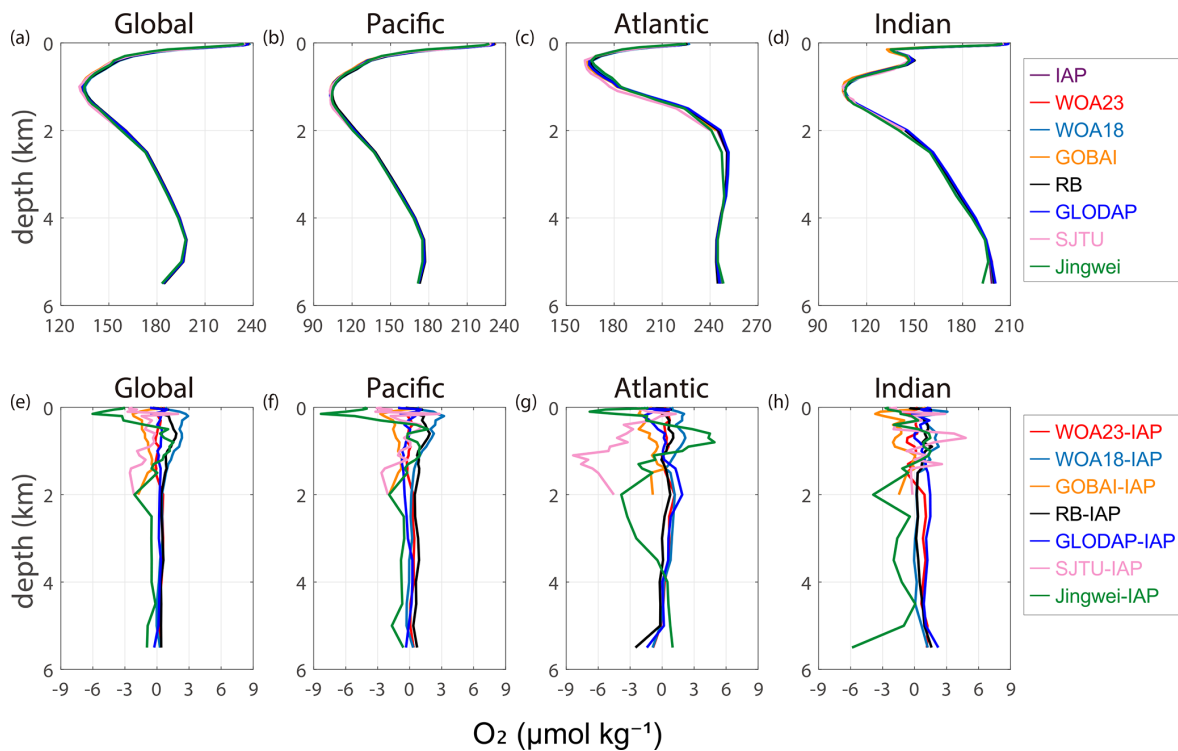


**Figure 3.** Area-weighted mean  $O_2$  climatology (a–d) and difference (e–h) relative to the IAP for the Global, Pacific, Atlantic, and Indian Oceans from ocean surface to 5500 m with a common ocean mask for different ocean basins in units of  $\mu\text{mol kg}^{-1}$ . The subplots for  $O_2$  climatology (a–d) use different scales.

$O_2$  decreases linearly with the decrease of latitude for all the datasets, except that for the high latitude range  $60\text{--}80^\circ\text{S}$ , the zonal mean  $O_2$  profiles maintain a relatively stable value and the estimations between different data products vary to an extent of  $\sim 20 \mu\text{mol kg}^{-1}$  (Fig. 4d), which illustrates the relatively higher uncertainty in the data reconstruction in this high latitude range.

### 3.3 Spatial pattern

The spatial distribution of the upper 1000 m mean  $O_2$  and the difference between IAP and six other datasets is shown in Fig. 5a–m. The dataset of Jingwei is not included because the spatial maps are not currently available. The difference of the 0–1000 m mean  $O_2$  is mainly within the magnitude of  $\sim 15 \mu\text{mol kg}^{-1}$ , which shows substantial local differences even though their differences are relatively small when averaged globally ( $\sim 3 \mu\text{mol kg}^{-1}$ , Fig. 3). The mean  $O_2$  of the GOBAI dataset is generally lower than IAP for 0–1000 m (Fig. 5f), consistent with the conclusions from the previous comparisons. There are bigger differences located in the regions such as the subpolar North Pacific, the Southern Ocean fronts, and the eastern Pacific regions close to OMZ boundaries, where the strong spatial  $O_2$  gradient, makes the reconstruction sensitive to the mapping process and data distribution (Ito et al., 2025). GOBAI, SJTU, and GLODAP show a

negative difference ( $\sim -15 \mu\text{mol kg}^{-1}$ ) compared to IAP for the upper 1000 m mean  $O_2$  in most of the north and equatorial Pacific Ocean, and equatorial Atlantic Ocean. WOA23 and GOBAI show a similar pattern of difference in the Indian and Pacific Oceans: more positive offsets in the eastern Pacific/Indian Oceans and negative offsets in the western Pacific/Indian Oceans. For the two generations of WOA products, the difference between WOA23 and IAP is more negative globally than the difference between WOA18 and IAP, likely due to the use of more recent data in WOA23. SJTU exhibits a distinct pattern of differences, with substantial negative differences occurring in the tropics.

The spatial map of the spread of the upper 1000 m mean climatological  $O_2$  among all the datasets except Jingwei is presented in Fig. 5n. The spread here is defined as the maximum absolute value of the differences between all the other products and IAP. The spread is within  $12 \mu\text{mol kg}^{-1}$  in most of the ocean areas, with the largest spread reaching  $25 \mu\text{mol kg}^{-1}$  where strong spatial  $O_2$  gradients exist. The spread is generally lower in the Southern Hemisphere than in the Northern Hemisphere, in contrast to the fact that there are more observations in the North. This might be related to three issues: (1) A common error in the mapping method, where the spatial interpolation generates over-smoothed or similar-biased fields in the Southern Hemisphere; (2) the variability is lower in the Southern Hemisphere than in the North-

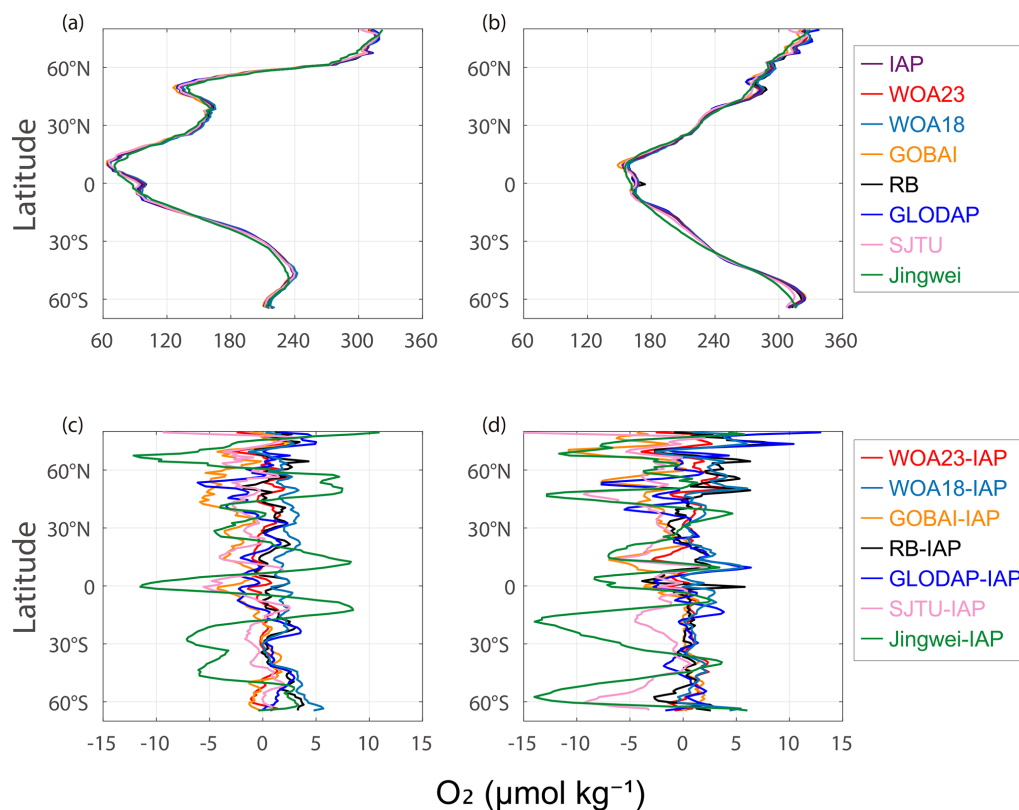


**Figure 4.** Global zonal mean  $O_2$  concentration and differences for 0–1000 m (**a, c**) and 0–100 m (**b, d**) (unit:  $\mu\text{mol kg}^{-1}$ ).

ern Hemisphere, which reduces the reconstruction errors in the Southern Hemisphere; (3) the deoxygenation trends are higher in the Northern Hemisphere than in the Southern thus the spread reveals the  $O_2$  level at different periods.

The exact reason can be explored with single-factor reconstruction experiments such as those performed by Ito et al. (2025), which use the same input data but different mapping methods to isolate the impact of mapping on climatology reconstruction. Further analyses are required, but it is useful to know the differences between the products. When comparing the depth-mean  $O_2$  between the eight datasets we adopted here which didn't distinguish different impact factors in the process of generating gridded data products and aimed to illustrate a comprehensive discrepancy, the difference for all the datasets for 0–300 m is within  $\pm 25 \mu\text{mol kg}^{-1}$  and the spread is up to  $35 \mu\text{mol kg}^{-1}$  (Fig. S3). The regions of high variability mainly locate in the tropical and East Pacific, subpolar North Pacific and Southern Ocean fronts where there are strong spatial  $O_2$  gradients. However, when using the same quality-controlled observational data as input and constraining the impact on data reconstruction to only the mapping method, the difference of the mapped  $O_2$  concentration between different mapping methods is within  $\pm 10 \mu\text{mol kg}^{-1}$  for 0–300 m (Ito et al., 2025). The overall difference between the data products is more than two times of the difference constrained to a single factor of the mapping

method, indicating that the other factors, such as the quality control technique, bias correction, vertical interpolation, and so on, also contribute to the uncertainty source to a large extent. Further analyses are required to assess and quantify the impact of every individual procedure on the whole process of  $O_2$  data reconstruction, but it is useful to know the differences between the data products as a start.

### 3.4 Annual cycle

The annual cycle of the four products that provide a monthly climatology (IAP, WOA23, WOA18, and GOBAI) is presented in Fig. 6 for the 0–100, 100–600, and 600–1500 m, and for Northern and Southern hemispheres, respectively calculated by the monthly anomalies derived by subtracting the annual mean climatology of every data product respectively. The annual cycle of the 0–100 m temperature for northern and southern hemispheres is also calculated using the gridded temperature climatology product of IAP (Cheng et al., 2024). The magnitude of the  $O_2$  seasonal cycle, defined as the maximum amplitude of the annual variation, is greatest near the surface and decreases with depth. Specifically, it is approximately  $6 \mu\text{mol kg}^{-1}$  for the 0–100 m layer and  $2 \mu\text{mol kg}^{-1}$  for the deeper layer (100–600 m). The reduced annual cycle with depth is associated with stronger annual variations

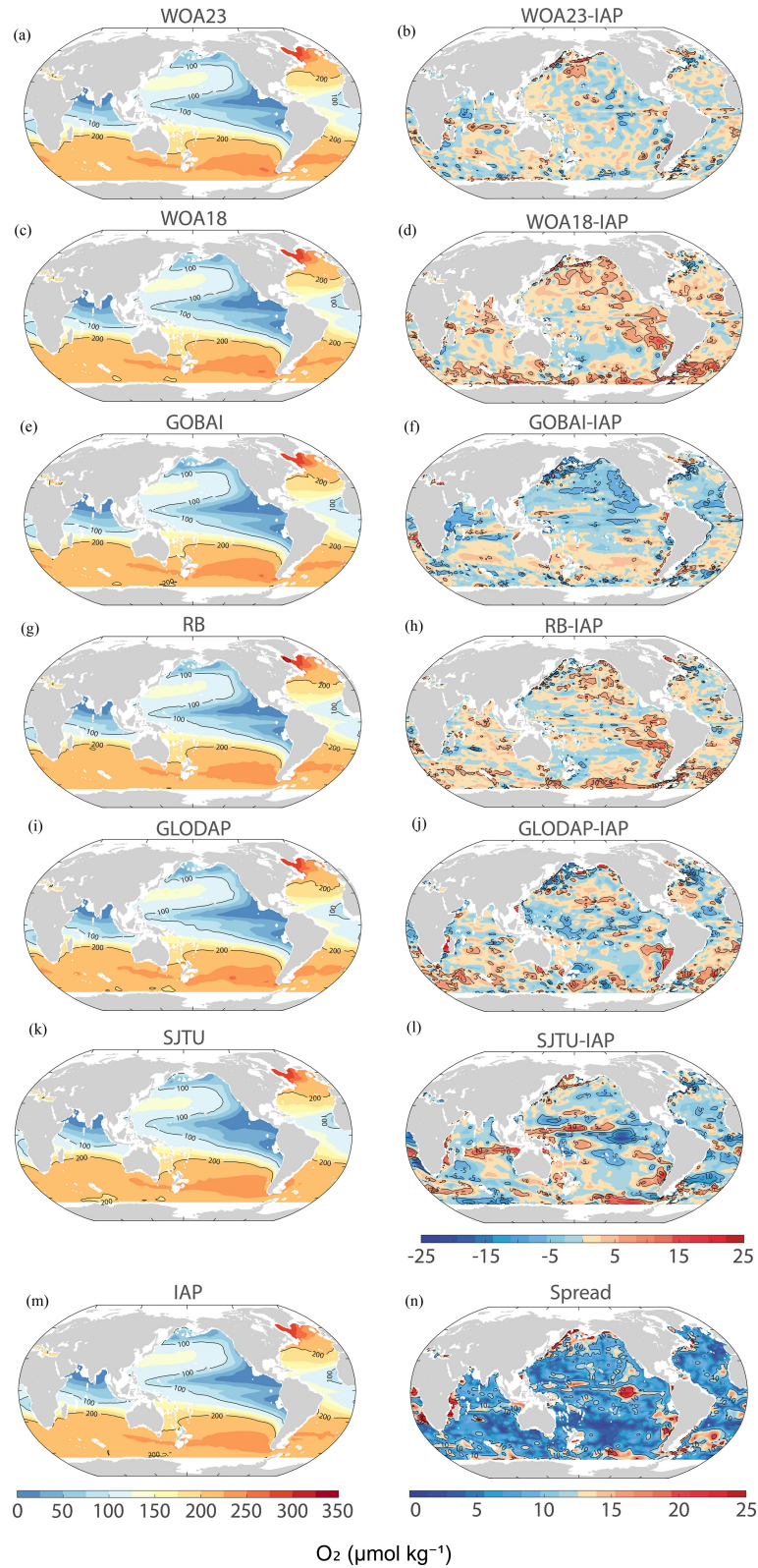


**Figure 5.** The spatial patterns of the upper 1000 m climatological mean  $O_2$  concentration (unit:  $\mu\text{mol kg}^{-1}$ ). (a) WOA23, (b) WOA23-IAP, (c) WOA18, (d) WOA18-IAP, (e) GOBAI, (f) GOBAI-IAP, (g) RB, (h) RB-IAP, (i) GLODAP, (j) GLODAP-IAP, (k) SJTU, (l) SJTU-IAP, (m) IAP, (n) Spread is calculated as the difference of the upper 1000 m climatological mean  $O_2$  among the datasets.

of ocean temperature, wind-driven ventilation, and biological processes in the upper ocean compared to the deep ocean.

The appearance time of maximum (April) and minimum (October)  $O_2$  levels in the northern hemisphere are consistent among the four datasets for 0–100 m global mean  $O_2$ . Moreover, the  $O_2$  maximum in the depth layer in the northern and southern hemispheres for 0–100 m lags about one month behind the temperature change, reflecting that besides the dominant thermal induced increase in  $O_2$  solubility, some physical/biological processes also impact the concentration of ocean  $O_2$  (Garcia et al., 2005b; Wang et al., 2022). For the northern hemisphere, the annual variation of the subsurface 100–600 m layer also shows a pattern of annual cycle with the maximum (April) and minimum (December) similar to the surface 0–100 m layer, indicating that the  $O_2$  annual cycle could penetrate to the deeper layer of  $\sim 600$  m. It is primarily due to the mechanisms including climatological winter mixed layer deepening, which ventilates the subsurface, and seasonal thermocline dynamics coupled with organic matter remineralization (Stramma et al., 2010). For the southern hemisphere, similar patterns also exist.

Although the two hemispheric  $O_2$  annual cycles can be well-defined, the global mean is more subtle, as different products show large differences in patterns of the global mean annual cycle (Fig. 7). It appears that global 100–600 m  $O_2$  annual cycles are more consistent across data products than 0–100 m, probably associated with noisier data and more natural variability near the sea surface. For global 100–600 m  $O_2$ , all datasets suggest an  $O_2$  reduction from March to September and an increase from October to February, consistent with the Southern Hemisphere changes (Fig. 7b versus Fig. 6b). The magnitude of the global 0–100 and 100–600 m annual cycle ranges from  $-1$  to  $0.8 \mu\text{mol kg}^{-1}$  for the four datasets, but the standard deviations among the four datasets are  $\sim 0.3 \mu\text{mol kg}^{-1}$  (0–100 m) and  $\sim 0.2 \mu\text{mol kg}^{-1}$  (100–600 m), indicating a similar level of signal and noise (Fig. 7).

The annual cycle of  $O_2$  anomalies shows a distinct spatial pattern (0–100 m mean  $O_2$ , April versus October, Fig. 8). The anomalies are calculated by subtracting the annual mean from the monthly climatologies for the four datasets (IAP, WOA23, WOA18, and GOBAI) respectively. In April, the  $O_2$  anomalies of 0–100 m in most of the northern hemisphere are positive, and they turn negative in October. The tropical ocean annual cycle is not easily defined, as many regions have semi-annual variability. Different products exhibit a consistent pattern of change, whereas the detailed structures are quite distinct. In general, WOA23 and WOA18 have more patchy characteristics than IAP and GOBAI, likely related to the mapping methods employed by each: WOA uses an anti-distance weighted function to interpolate the field; on the other hand, IAP uses model simulations to provide covariance and GOBAI takes advantage of correlations between  $O_2$  and temperature and salinity, both building physical ocean properties into the reconstruction.

The zonal mean structure of the annual cycle is shown in Fig. 9, and all the datasets show similar annual cycle patterns with some difference in smoothness and magnitude for both 0–100 and 100–600 m mean  $O_2$ . For 0–100 m, the largest seasonal changes occur in the extra-tropics in the 30 to 60° N belts of the Northern hemisphere. In the Southern hemisphere, the largest seasonal changes occur in the latitudinal band centered near 40° S. For both 0–100 and 100–600 m, the phase transitions occur around July and January for all datasets, which are consistent with the annual variation analysis in Fig. 6. The phase change of  $O_2$  lags about one month behind the temperature change (June and December as shown in Fig. S4), reflecting that some physical/biological processes also impact the concentration of  $O_2$  besides the dominant thermally induced increase in  $O_2$  solubility. Semi-annual cycles near the equator are visible in the upper ocean for almost all products. There is a distinction of the annual cycle at about 10° N, corresponding to the location of the intertropical convergence zone (ITCZ) (Garcia et al., 2005b).

The zonal mean annual cycles of solubility and Apparent Oxygen Utilization (AOU) of different data products for 0–100 and 100–600 m are shown in Fig. 10. The solubility is calculated using the gridded temperature and salinity products of IAP (Cheng et al., 2024) following the Garcia and Gordon (1992) method. Generally, the zonal 0–100 m  $O_2$  seasonal cycle is mainly dominated by the solubility, whereas the AOU dominates the 100–600 m  $O_2$  pattern.

For 0–100 m, the AOU seasonal cycle in the mid-latitude is about two to three months lagging that of the temperature/solubility seasonal variation (Figs. 6, 10, S4). Within 20–60° N, the zonal mean AOU anomaly of 0–100 m is mostly negative from March to August. The phase transition of AOU occurs in March, which corresponds to the temperature minimum/solubility maximum. And AOU reaches a minimum in about May/June, corresponding to the phase transition of the zonal mean temperature/solubility anomaly (Figs. S4, 10). A possible explanation is from the combined impacts of biological and physical processes (Garcia et al., 2005a). The spring phytoplankton bloom lags the onset of temperature increase (starting in March) because phytoplankton proliferation requires sufficient light from increasing spring insolation and nutrient entrainment due to a shallower mixed layer (Martin, 2012). And the net community production (NCP, the difference between gross community photosynthesis and community respiration) reaches a maximum in about May (Wang et al., 2022). The solubility reaches a minimum in September, which corresponds with the phase change of AOU. And the maximum of AOU lags about two months behind the temperature maximum/solubility minimum, which is also a combined effect of the prolonged response time of biological processes and the physical processes possibly induced by the deepening autumn mixed layer. The situation in 20–60° S is similar to 20–60° N for 0–100 m, mainly with the signs reversed. For 100–600 m, the annual variation in temperature/solubility is relatively small, and the pattern of AOU

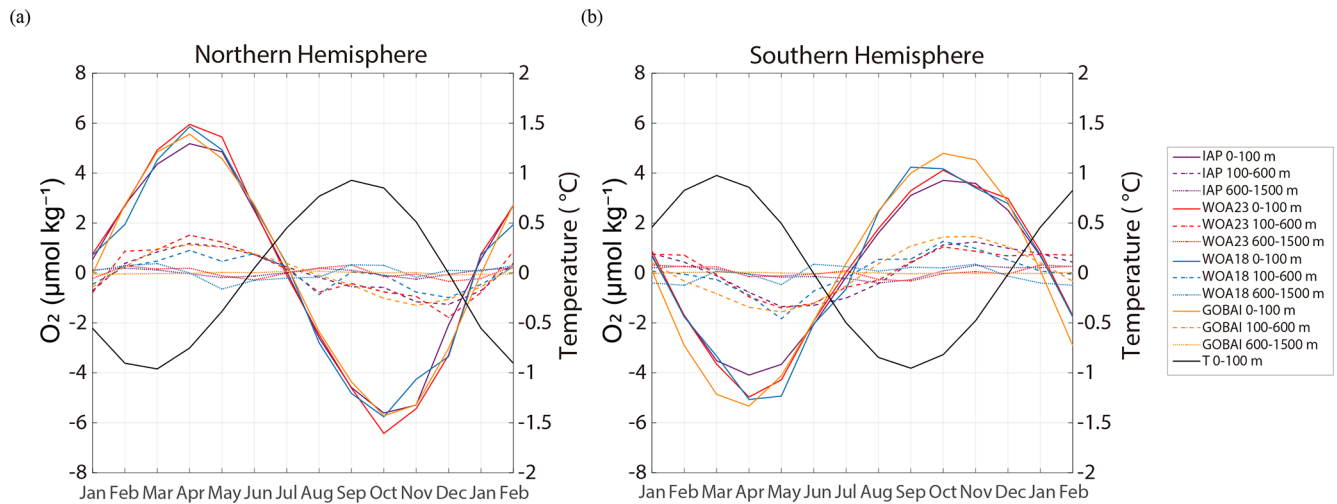


**Figure 6.** Annual variation of the (a) Northern Hemisphere and (b) Southern Hemisphere global mean O<sub>2</sub> for IAP, WOA23, WOA18, and GOBAI datasets.

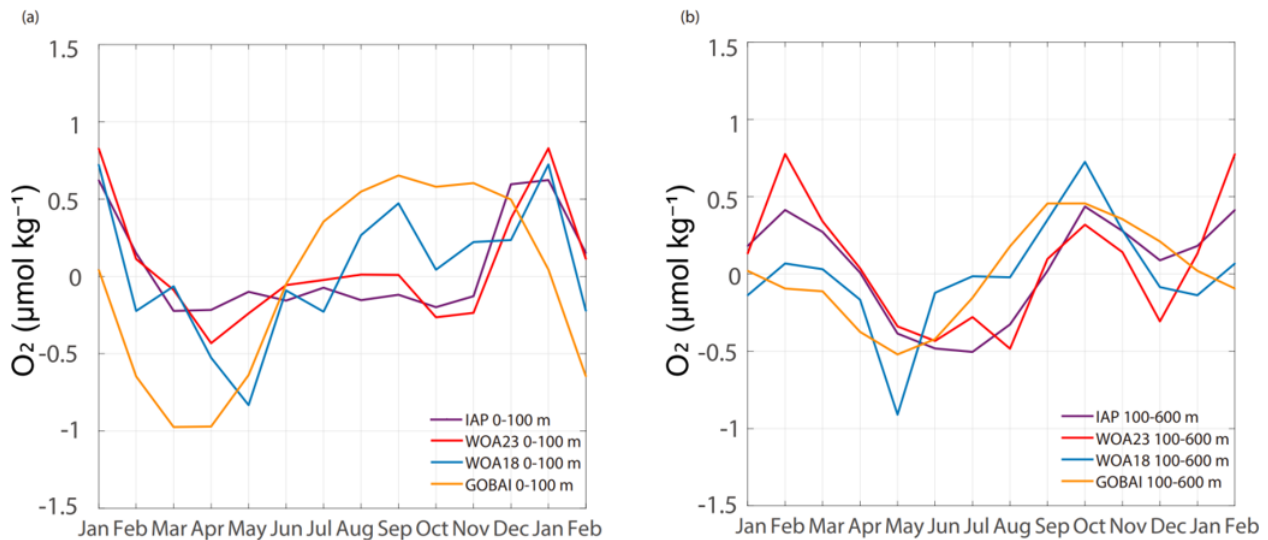


**Figure 7.** Global annual variation of the (a) 0–100 m and (b) 100–600 m global mean O<sub>2</sub> for IAP, WOA23, WOA18, and GOBAI datasets.

variation dominates, with the underlying processes requiring further investigation.

To assess the patterns of annual cycle regionally, the zonal mean structures of the annual cycle for different ocean basins are shown in Figs. S5–S7. Distinct seasonal changes exist in the Pacific, Atlantic and Indian Oceans. The annual cycle patterns for the Pacific and Atlantic Ocean coincide with the global O<sub>2</sub> annual cycle both for the 0–100 and 100–600 m layers closely. For the Indian Ocean, there are larger seasonal changes in the latitude range of  $\sim 10$ – $20^\circ$  N for 0–100 m than the Pacific and Atlantic Oceans. The annual variations of the mean O<sub>2</sub> for three major ocean basins (Pacific, Atlantic, Indian) for 0–100 and 100–600 m are shown in Figs. S8–S10, and also for the North and South Pacific/Atlantic, respectively, in Figs. S11–S12. The magnitude of the O<sub>2</sub> sea-

sonal cycle is greatest in the Atlantic Ocean ( $\sim 3 \mu\text{mol kg}^{-1}$ ) for the 0–100 m layer, which corresponds to a magnitude of  $\sim 6 \mu\text{mol kg}^{-1}$  in the North Atlantic and  $\sim 4 \mu\text{mol kg}^{-1}$  in the South Atlantic. The minimum and maximum O<sub>2</sub> levels ( $-4$  to  $6 \mu\text{mol kg}^{-1}$ ) and also occurrence time (July/October) of WOA18 for 0–100 m differ the most from those of the other three datasets in the South Atlantic (Fig. S12b).

### 3.5 Oxygen minimum zones

Oxygen minimum zones (OMZ) are important regions that impact marine organism distributions and biogeochemical cycling. OMZ occur in various regions such as the tropical Pacific and Atlantic Oceans, the North Pacific Ocean, and the North Indian Ocean, posing challenges for marine organ-

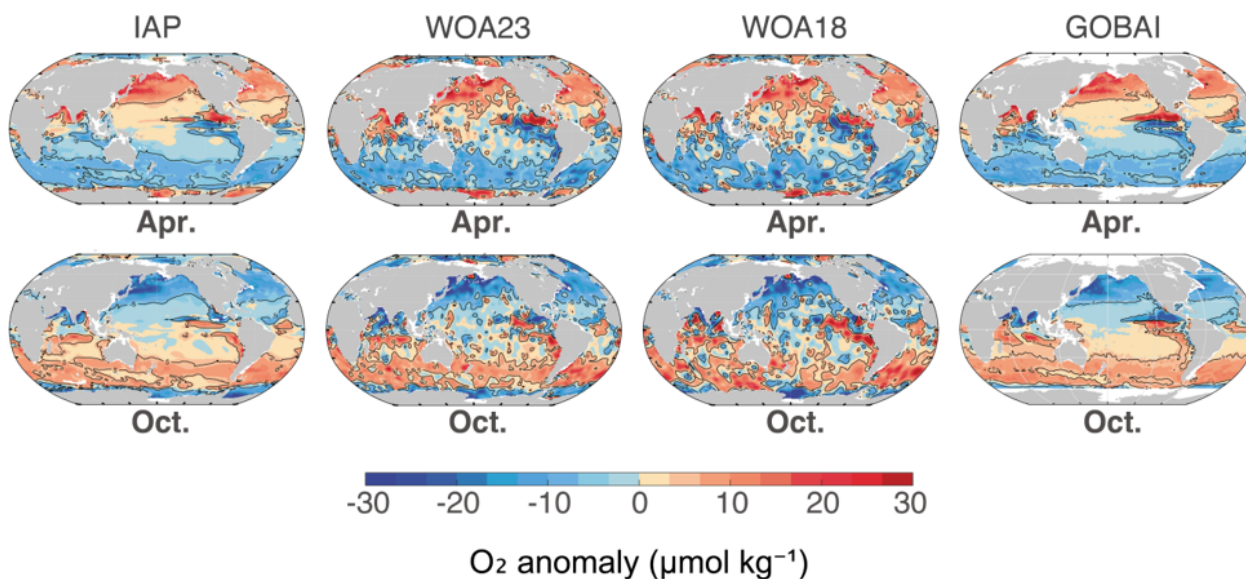


**Figure 8.** Spatial distribution of the O<sub>2</sub> anomaly (0–100 m) for the IAP, WOA23, WOA18, and GOBAI climatology.

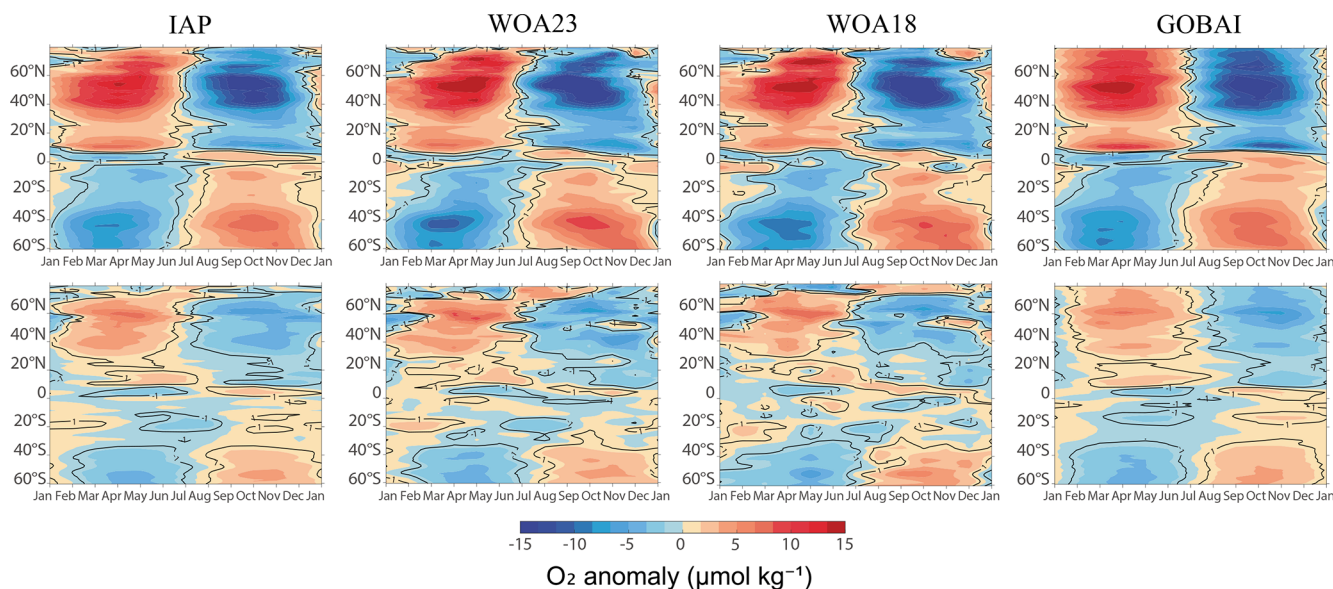


**Figure 9.** Zonal mean annual cycles for 0–100 m (upper) and 100–600 m (lower) for different data products (IAP, WOA23, WOA18, and GOBAI).

isms adapted to higher O<sub>2</sub> concentrations (Stramma et al., 2008, 2021). In various studies, OMZ are bounded by different thresholds of O<sub>2</sub> levels. Here, we select two typical thresholds of 60 and 90  $\mu\text{mol kg}^{-1}$  to define OMZ (Ito et al., 2025), referred to as OMZ60 and OMZ90, respectively.

The zonal mean O<sub>2</sub> of the IAP climatology dataset for global and three major basins are shown in Fig. 11. Globally, the zonal mean OMZ90 regions are mainly located within 200–1200 m and 5° S–30° N, associated with upwelling and high O<sub>2</sub> consumption. The Pacific Ocean contains the largest volume of OMZ60 and OMZ90 among the three ocean

basins, with the OMZ90 extending from  $\sim 15^\circ$  S to  $\sim 60^\circ$  N and from a depth of  $\sim 200$  to  $\sim 3000$  m. There is a gradual increase in the max depth of OMZ90 and OMZ60 in the Pacific Ocean from  $\sim 15^\circ$  S to  $\sim 60^\circ$  N; thus, the OMZ in the North Pacific Ocean has greater vertical extent. The OMZ in the North Pacific Ocean is also more severe because there is a notable region with zonal O<sub>2</sub> levels less than 30  $\mu\text{mol kg}^{-1}$  in the  $\sim 700$  to  $\sim 1500$  m layer. The OMZ90 in the Indian Ocean extends from  $\sim 10^\circ$  S to the northernmost end and is located from  $\sim 20$  down to a maximum depth of 1800 m. In the Atlantic Ocean, the OMZ90 is located within a 300–

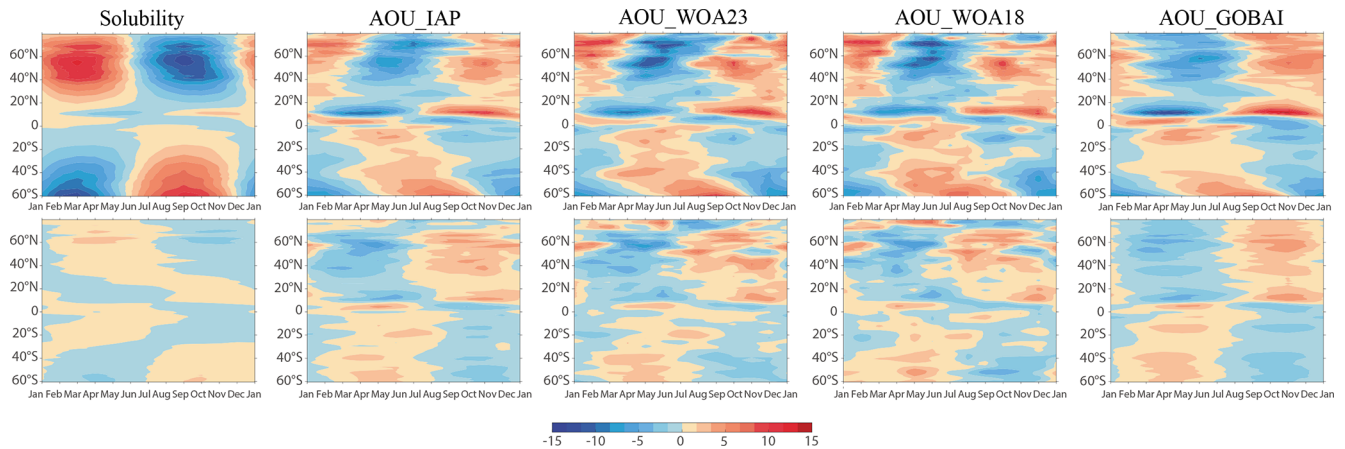


**Figure 10.** Zonal mean annual cycles of the solubility and AOU anomaly of different data products (AOU\_IAP, AOU\_WOA23, AOU\_WOA18, and AOU\_GOBAl) for 0–100 m (upper) and 100–600 m (lower) (unit:  $\mu\text{mol kg}^{-1}$ ).

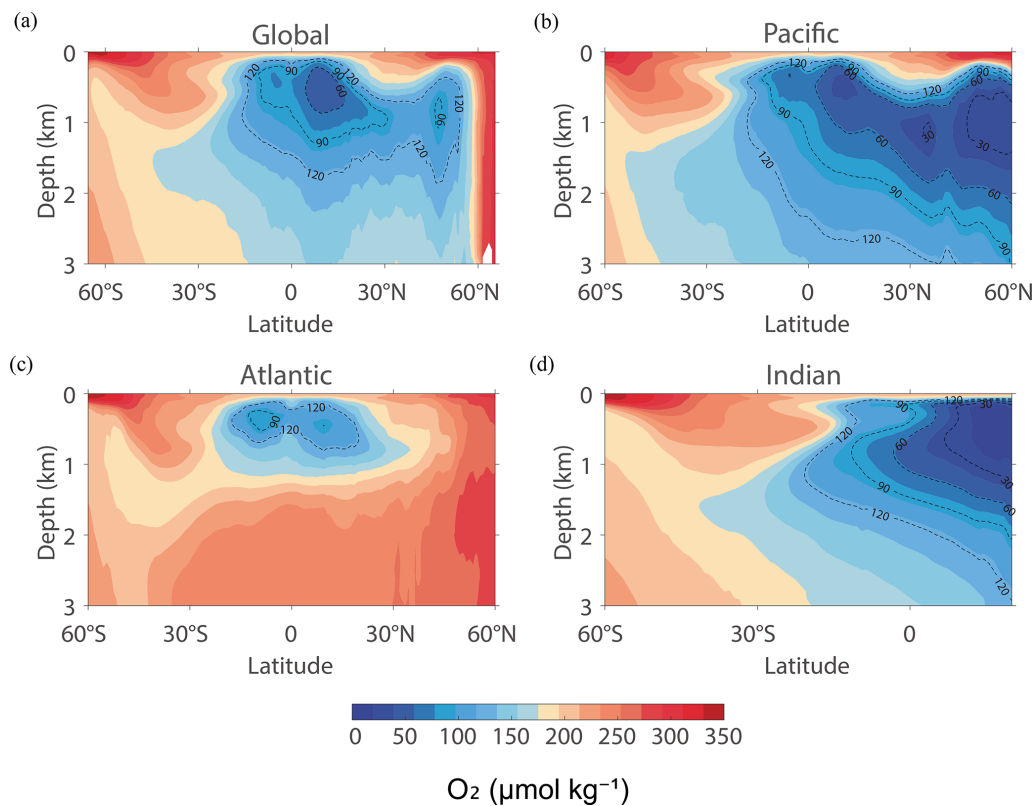


**Figure 11.** Comparison of zonal mean  $\text{O}_2$  climatology (IAP climatology, unit:  $\mu\text{mol kg}^{-1}$ ) in the (a) Global Ocean, (b) Pacific, (c) Atlantic, and (d) Indian Oceans.

500 m layer, with an area much smaller than that of the Pacific and Indian Oceans (Table 2).

We also calculated the volume of OMZ60 and OMZ90 globally and for each basin in Table 2 using six datasets (excluding GOBAI and SJTU because their maximum depth only reaches about 2000 m below the ocean surface). The global volume of OMZ60 and OMZ90 is generally consistent

among the datasets, with a standard deviation of 1.95 % and 1.72 % across the products for OMZ60 and OMZ90, respectively. The Pacific Ocean contains most of the OMZ (83.05 % of the global OMZ60 and 81.29 % of the global OMZ90), with a standard deviation of 3.93 % and 2.37 % across the products. The Atlantic Ocean contains about 1.04 % and 2.38 % of the global OMZ60 and OMZ90, respectively,

**Table 2.** The volume of OMZ60 and OMZ90 calculated from the annual mean climatology for each basin and for different products. The values are in the units of  $10^6 \text{ km}^3$ .

Datasets	OMZ60				OMZ90			
	Global	Pacific	Atlantic	Indian	Global	Pacific	Atlantic	Indian
IAP	81.76	68.98	0.85	11.91	152.78	125.56	3.83	23.36
WOA23	83.79	69.90	0.88	12.49	155.46	126.86	3.72	24.33
WOA18	79.42	66.71	0.74	11.46	152.23	124.93	3.50	23.28
RB	80.93	67.73	0.94	11.74	152.69	124.95	3.93	23.26
GLODAP	80.68	68.18	1.07	11.42	146.69	119.85	3.93	22.90
Jingwei	78.99	61.74	0.52	12.63	152.14	119.19	2.81	23.70
Mean	80.92	67.21	0.84	11.94	152.00	123.56	3.62	23.47
Standard Deviation	1.58	2.64	0.17	0.47	2.62	2.93	0.39	0.45

which is the lowest among the three ocean basins. The standard deviation is 20.24 % and 10.77 % for the Atlantic Ocean OMZ60 and OMZ90, respectively. The estimated OMZ for the Atlantic Ocean may be more sensitive to the horizontal resolution, mapping method, and so on.

The OMZ areas as a function of depth and density are shown in Fig. 12. The density layers are calculated with the Gibbs-SeaWater Oceanographic Toolbox (IOC et al., 2010; McDougall and Barker, 2011; Kwiecinski and Babin, 2021), using the gridded temperature and salinity climatology products of IAP (Cheng et al., 2024). The maximum OMZ60 area occurs at a depth of  $\sim 800 \text{ m}$  and a density of  $27.75 \text{ kg m}^{-3}$  for all the datasets. Most OMZ60s exist in the upper 2000 m. So that all the climatologies including GOBAI and SJTU with the maximum depth of 2000 m could be involved in the analysis of OMZ areas at depth levels. GOBAI and SJTU exhibit a larger OMZ60 volume within the upper 2000 m compared to other products, and the maximum depth of SJTU OMZ60 is  $\sim 1700 \text{ m}$ , which is shallower than that of the other products. At density levels, the products are very consistent, and SJTU shows a larger area of OMZ60 near the  $27.4 \text{ kg m}^{-3}$  level and Jingwei shows a smaller area of OMZ60 near the  $27 \text{ kg m}^{-3}$  level.

Figure 11a–c shows the horizontal OMZ60 area at depth levels for the Pacific, Atlantic, and Indian Oceans, respectively. Consistent with the volume assessment in Table 2, the Pacific Ocean contains the largest OMZ60 area, followed by the Indian and Atlantic Oceans. The maximum OMZ60 area occurs at a depth of about 800 m in the Pacific and Indian Oceans, but at a much shallower depth of  $\sim 400 \text{ m}$  in the Atlantic Ocean. Jingwei shows the largest difference from the other products in the Pacific and Indian Oceans at the upper 500 m depth. SJTU shows a larger area of OMZ60 in the Pacific and Indian Oceans but a smaller area in the Atlantic Ocean than the other products (Fig. 13). Collectively, different products show a spread of  $\pm 4 \times 10^6 \text{ km}^2$  for the Pacific OMZ60 and of  $\pm 1 \times 10^6 \text{ km}^2$  for the Indian and Atlantic OMZ60 (Fig. 13d–f), except that Jingwei shows a very large difference of up to  $-9 \times 10^6 \text{ km}^2$  at the depth around 500 m

for the Pacific OMZ60 area compared to the ensemble mean (Fig. 13d).

#### 4 Conclusions

Observationally-based gridded data products provide a basis for detecting and understanding ocean  $\text{O}_2$  changes at various spatial and temporal scales. These observational datasets are also used to validate the computational ocean biogeochemistry and earth system models. This study provides a quantitative description of the  $\text{O}_2$  climatology, annual cycle, and OMZ distribution with eight  $\text{O}_2$  data products. There have been several new  $\text{O}_2$  data products developed in recent years, which makes this comparative analysis timely.

The global mean  $\text{O}_2$  shows a well-established high-low-high vertical structure and a good consistency among all products. The global mean  $\text{O}_2$  concentrations of the products over depth generally agree within  $\pm 3 \mu\text{mol kg}^{-1}$ . Regionally, the gridded mean difference of the 0–1000 m mean  $\text{O}_2$  is mainly within  $\sim 12 \mu\text{mol kg}^{-1}$ . For the global 0–100 m  $\text{O}_2$  annual cycle,  $\text{O}_2$  anomalies (differences from the annual mean) ranges from  $-1$  to  $0.8 \mu\text{mol kg}^{-1}$ , but the inter-products difference (defined by the standard deviation of four datasets that provide a monthly climatology) can be as large as  $\sim 0.3 \mu\text{mol kg}^{-1}$ , indicating a similar signal-to-noise ratio among the four datasets of monthly climatology. We also analyzed the OMZ distribution for different climatology datasets. Different products show a spread of  $\pm 4 \times 10^6 \text{ km}^2$  for the Pacific OMZ60 and  $\pm 1 \times 10^6 \text{ km}^2$  for the Indian and Atlantic OMZ60.

The assessments presented in this study demonstrate the consistency and differences among available products, supporting their future use. Substantial local differences ( $\pm 25 \mu\text{mol kg}^{-1}$  for the upper 1000 m climatological mean) can be seen, which could influence the baseline from which anomalies and trends are calculated and could give an insight into regions that are relatively more sensitive in the process of gridded data reconstruction, such as the subpolar North

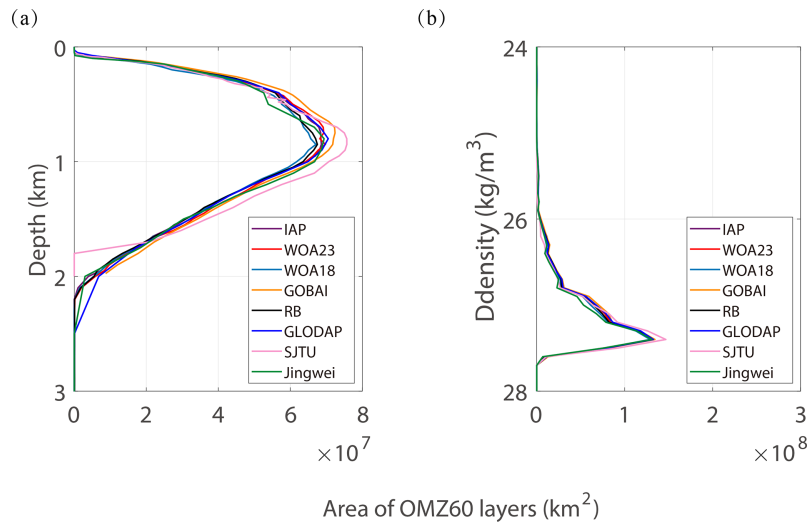


**Figure 12.** The global horizontal area of OMZ60 in each interpolated layer with respect to depth and (b) density.

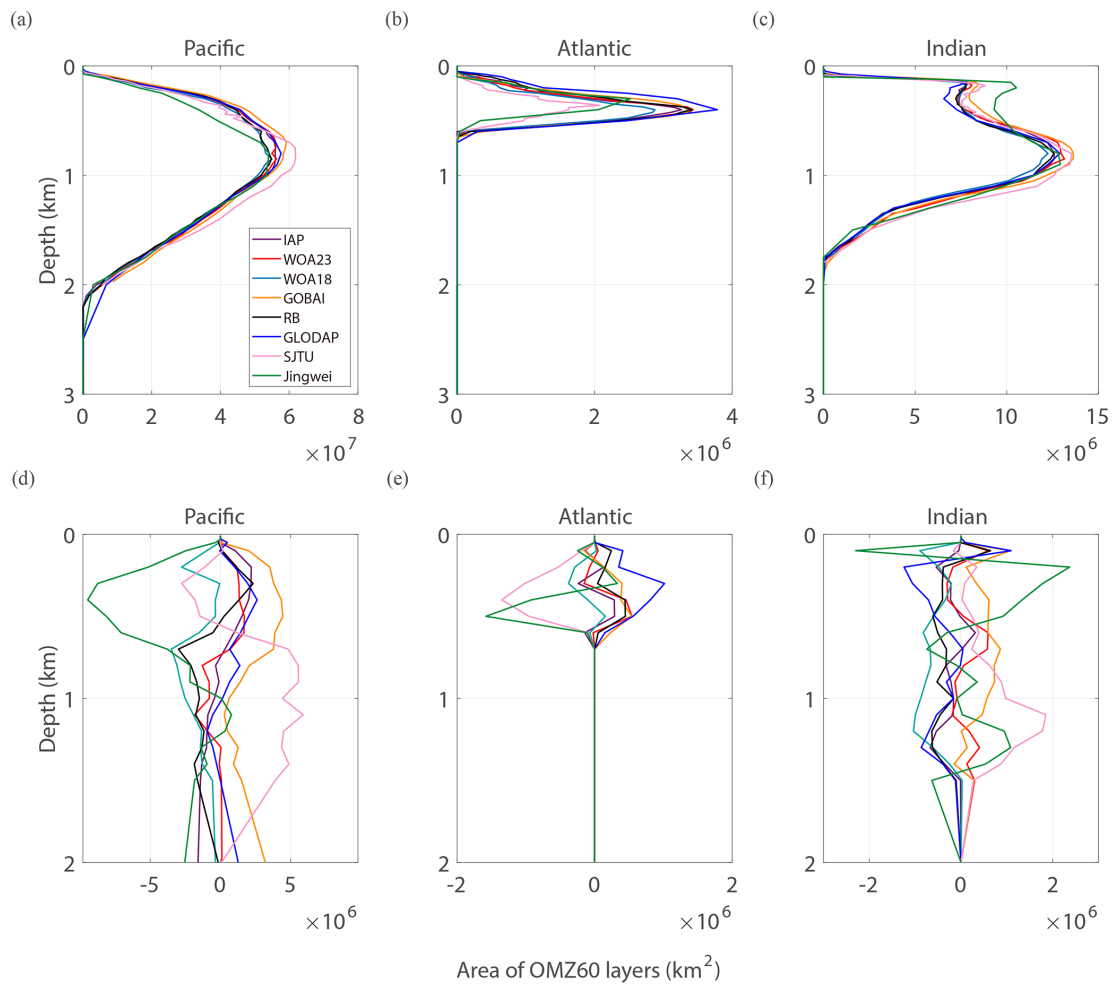


**Figure 13.** OMZ60 area for the Pacific, Atlantic, and Indian Oceans in units of  $10^6 \text{ km}^2$ . The upper row is the vertical distribution of the OMZ areas: (a) Pacific, (b) Atlantic, (c) Indian. The lower row is the differences in the OMZ areas relative to the ensemble mean: (d) Pacific, (e) Atlantic, (f) Indian.

Pacific, the Southern Ocean fronts, and the eastern Pacific regions close to OMZ boundaries where the spatial O<sub>2</sub> gradient is large.

The overall spread across products results from all uncertainty sources (e.g., measurement errors, mapping errors, different time periods, etc.). Controlled intercomparisons that isolate each uncertainty source are needed in the future to understand the contribution of a single factor, especially in regions showing a large spread. It will eventually help the community to improve the methodologies and reduce the spread in the future. Another caveat is that only a limited number of products are included in this inter-comparison. We hope to maintain and extend this activity in the future and serve as a regular intercomparison exercise to provide critical information to the data users.

*Data availability.* All the gridded data products used in this study are available at <https://doi.org/10.5281/zenodo.16664650> (GODIP-DO Group, 2025).

*Supplement.* The supplement related to this article is available online at <https://doi.org/10.5194/os-22-1483-2026-supplement>.

*Author contributions.* JD and LC-conceptualization, supervision, methodology; JD-formal analysis, visualization, writing; JD, LC, HEG, ZW, JDS, CJR, YZ and BL-data curation; TI, HEG, ZW, JDS, GGN, SMB and SM-writing.

*Competing interests.* The contact author has declared that none of the authors has any competing interests.

*Disclaimer.* Publisher's note: Copernicus Publications remains neutral with regard to jurisdictional claims made in the text, published maps, institutional affiliations, or any other geographical representation in this paper. The authors bear the ultimate responsibility for providing appropriate place names. Views expressed in the text are those of the authors and do not necessarily reflect the views of the publisher.

*Acknowledgements.* We are thankful to NCEI, NOAA and the Global Data Assembly Centers (GDAC) for providing access to the observation data used in this study. We also thank two reviewers for their detailed and constructive comments.

*Financial support.* IAP authors gratefully acknowledge support by National Natural Science Foundation of China (grant no. 42261134536), the new Cornerstone Science Foundation through the XPLOER PRIZE and the Asian Cooperation Fund, and the International Partnership Program of the Chinese Academy of Sciences (grant no. 060GJHZ2024064MI). TI and JDS are supported

by funding from the US National Science Foundation (grant nos. OCE-2446011, 2446012). This is CICOES contribution no. 2025-1474 and PMEL contribution no. 5797.

*Review statement.* This paper was edited by Maribel I. García-Ibáñez and reviewed by Malek Belgacem and one anonymous referee.

## References

- Bindoff, N. L., Cheung, W. W. L., Kairo, J. G., Arístegui, J., Guinder, V. A., Hallberg, R., Hilmi, N., Jiao, N., Karim, M. S., Levin, L., O'Donoghue, S., Purca Cuicapusa, S. R., Rinkevich, B., Suga, T., Tagliabue, A., and Williamson, P.: Changing Ocean, marine ecosystems, and dependent communities, In: IPCC Special Report on the Ocean and Cryosphere in a Changing Climate, Cambridge University Press, Cambridge, UK and New York, NY, USA, 447–587, <https://doi.org/10.1017/9781009157964.007>, 2019.
- Boyer, T. P., Baranova, O. K., Coleman, C., Garcia, H. E., Grodsky, A., Locarnini, R. A., Mishonov, A. V., Paver, C. R., Reagan, J. R., Seidov, D., Smolyar, I. V., Weathers, K., and Zweng, M. M.: World Ocean Database 2018, Mishonov, A. V., Technical Editor, NOAA Atlas NESDIS 87, [https://www.ncei.noaa.gov/sites/default/files/2020-04/wod\\_intro\\_0.pdf](https://www.ncei.noaa.gov/sites/default/files/2020-04/wod_intro_0.pdf) (last access: 8 May 2026), 2018.
- Breitbart, D., Levin, L. A., Oschlies, A., Grégoire, M., Chavez, F. P., Conley, D. J., Garçon, V., Gilbert, D., Gutiérrez, D., Isensee, K., Jacinto, G. S., Limburg, K. E., Montes, I., Naqvi, S. W. A., Pitcher, G. C., Rabalais, N. N., Roman, M. R., Rose, K. A., Seibel, B. A., Telszewski, M., Yasuhara, M., and Zhang, J.: Declining oxygen in the global ocean and coastal waters, *Science*, 359, eaam7240, <https://doi.org/10.1126/science.aam7240>, 2018.
- Cheng, L. and Zhu, J.: Benefits of CMIP5 Multimodel Ensemble in Reconstructing Historical Ocean Subsurface Temperature Variations, *J. Climate*, 29, 5393–5416, <https://doi.org/10.1175/JCLI-D-15-0730.1>, 2016.
- Cheng, L., Trenberth, K. E., Fasullo, J., Boyer, T., Abraham, J., and Zhu, J.: Improved estimates of ocean heat content from 1960 to 2015, *Sci. Adv.*, 3, e1601545, <https://doi.org/10.1126/sciadv.1601545>, 2017.
- Cheng, L., Pan, Y., Tan, Z., Zheng, H., Zhu, Y., Wei, W., Du, J., Yuan, H., Li, G., Ye, H., Gouretski, V., Li, Y., Trenberth, K. E., Abraham, J., Jin, Y., Reseghetti, F., Lin, X., Zhang, B., Chen, G., Mann, M. E., and Zhu, J.: IAPv4 ocean temperature and ocean heat content gridded dataset, *Earth Syst. Sci. Data*, 16, 3517–3546, <https://doi.org/10.5194/essd-16-3517-2024>, 2024.
- Deutsch, C., Brix, H., Ito, T., Frenzel, H., and Thompson, L.: Climate-forced variability of ocean hypoxia, *Science*, 333, 336–339, <https://doi.org/10.1126/science.1202422>, 2011.
- Garcia, H. E. and Gordon, L. I.: Oxygen solubility in seawater: Better fitting equations, *Limnol. Oceanogr.*, 37, 1307–1312, <https://doi.org/10.4319/lo.1992.37.6.1307>, 1992.
- Garcia, H. E., Boyer, T. P., Levitus, S., Locarnini, R. A., and Antonov, J.: On the variability of dissolved oxygen and apparent oxygen utilization content for the upper world

- ocean: 1955 to 1998, *Geophys. Res. Lett.*, 32, L09604, <https://doi.org/10.1029/2004GL022286>, 2005a.
- Garcia, H. E., Boyer, T. P., Levitus, S., Locarnini, R. A., and Antonov, J.: Climatological annual cycle of upper ocean oxygen content anomaly, *Geophys. Res. Lett.*, 32, L05611, <https://doi.org/10.1029/2004GL021745>, 2005b.
- Garcia, H. E., Weathers, K., Paver, C. R., Smolyar, I., Boyer, T. P., Locarnini, R. A., Zweng, M. M., Mishonov, A. V., Baranova, O. K., Seidov, D., and Reagan, J. R.: World Ocean Atlas 2018, Volume 3: Dissolved Oxygen, Apparent Oxygen Utilization, and Oxygen Saturation, edited by: Mishonov, A., NOAA Atlas NESDIS 83, [https://www.ncei.noaa.gov/sites/default/files/2020-04/woa18\\_vol3.pdf](https://www.ncei.noaa.gov/sites/default/files/2020-04/woa18_vol3.pdf), 2018.
- Garcia, H. E., Wang, Z., Bouchard, C., Cross, S. L., Paver, C. R., Reagan, J. R., Boyer, T. P., Locarnini, R. A., Mishonov, A. V., Baranova, O. K., Seidov, D., and Dukhovskoy, D.: World Ocean Atlas 2023, Volume 3: Dissolved Oxygen, Apparent Oxygen Utilization, Dissolved Oxygen Saturation, and 30-year Climate Normal, A. Mishonov Technical Editor, NOAA Atlas NESDIS 91, 100 pp., <https://doi.org/10.25923/rb67-ns53>, 2024.
- Garcia-Soto, C., Cheng, L., Caesar, L., Schmidtko, S., Jewett, E. B., Cheripka, A., Rigor, I., Caballero, A., Chiba, S., Báez, J. C., Zielinski, T., and Abraham, J. P.: An Overview of Ocean Climate Change Indicators: Sea Surface Temperature, Ocean Heat Content, Ocean pH, Dissolved Oxygen Concentration, Arctic Sea Ice Extent, Thickness and Volume, Sea Level and Strength of the AMOC (Atlantic Meridional Overturning Circulation), *Front. Mar. Sci.*, 8, 642372, <https://doi.org/10.3389/fmars.2021.642372>, 2021.
- GODIP-DO Group: Global Dissolved Oxygen Gridded Climatological Datasets, Zenodo [data set], <https://doi.org/10.5281/zenodo.16664650>, 2025.
- Gouretski, V., Cheng, L., Du, J., Xing, X., and Chai, F.: A quality-controlled and bias-adjusted global ocean oxygen profile dataset, Marine Science Data Center of the Chinese Academy of Sciences [data set], <https://doi.org/10.12157/IOCAS.20231208.001>, 2024a.
- Gouretski, V., Cheng, L., Du, J., Xing, X., Chai, F., and Tan, Z.: A consistent ocean oxygen profile dataset with new quality control and bias assessment, *Earth Syst. Sci. Data*, 16, 5503–5530, <https://doi.org/10.5194/essd-16-5503-2024>, 2024b.
- Grégoire, M., Garçon, V., Garcia, H., Breitburg, D., Isensee, K., Oschlies, A., Telszewski, M., Barth, A., Bittig, H. C., Carstensen, J., Carval, T., Chai, F., Chavez, F., Conley, D., Coppola, L., Crowe, S., Currie, K., Dai, M., Deflandre, B., Dewitte, B., Diaz, R., Garcia-Robledo, E., Gilbert, D., Giorgetti, A., Glud, R., Gutierrez, D., Hosoda, S., Ishii, M., Jacinto, G., Langdon, C., Lauvset, S. K., Levin, L. A., Limburg, K. E., Mehrtens, H., Montes, I., Naqvi, W., Paulmier, A., Pfeil, B., Pitcher, G., Pouliquen, S., Rabalais, N., Rabouille, C., Recape, V., Roman, M., Rose, K., Rudnick, D., Rummer, J., Schmechtig, C., Schmidtko, S., Seibel, B., Slomp, C., Sumalia, U. R., Tanhua, T., Thierry, V., Uchida, H., Wanninkhof, R., and Yasuhara, M.: A Global Ocean Oxygen Database and Atlas for Assessing and Predicting Deoxygenation and Ocean Health in the Open and Coastal Ocean, *Front. Mar. Sci.*, 8, 1–29, <https://doi.org/10.3389/fmars.2021.724913>, 2021.
- Gulev, S. K., Thorne, P. W., Ahn, J., Dentener, F. J., Domingues, C. M., Gerland, S., Gong, D., Kaufman, D. S., Nnamchi, H. C., Quaas, J., Rivera, J. A., Sathyendranath, S. L., Smith, S. L., Trewin, B., von Schuckmann, K., and Vose, R. S.: Changing State of the Climate System, in: *Climate Change 2021: The Physical Science Basis. Contribution of Working Group I to the Sixth Assessment Report of the Intergovernmental Panel on Climate Change*, edited by: Masson-Delmotte, V., Zhai, P., Pirani, A., Connors, S. L., Péan, C., Berger, S., Caud, N., Chen, Y., Goldfarb, L., Gomis, M. I., Huang, M., Leitzell, K., Lonnoy, E., Matthews, J. B. R., Maycock, T. K., Waterfield, T., Yelekçi, O., Yu, R., and Zhou, B., Cambridge University Press, Cambridge, United Kingdom and New York, NY, USA, 287–422, <https://doi.org/10.1017/9781009157896.004>, 2021.
- Huang, S., Shao, J., Chen, Y., Qi, J., Wu, S., Zhang, F., He, X., and Du, Z.: Reconstruction of dissolved oxygen in the Indian Ocean from 1980 to 2019 based on machine learning techniques, *Front. Mar. Sci.*, 10, 1291232, <https://doi.org/10.3389/fmars.2023.1291232>, 2023.
- IOC, SCOR, and IAPSO: The International thermodynamic equation of seawater-2010: Calculation and use of thermodynamic properties, Intergovernmental Oceanographic Commission, Manuals and Guides No. 56, UNESCO, [https://www.teos-10.org/pubs/TEOS-10\\_Manual.pdf](https://www.teos-10.org/pubs/TEOS-10_Manual.pdf) (last access: 8 May 2026), 2010.
- Ito, T., Minobe, S., Long, M. C., and Deutsch, C.: Upper ocean O<sub>2</sub> trends: 1958–2015, *Geophys. Res. Lett.*, 44, 4214–4223, <https://doi.org/10.1002/2017GL073613>, 2017.
- Ito, T., Cervania, A., Cross, K., Ainchwar, S., and Delawalla, S.: Mapping dissolved oxygen concentrations by combining shipboard and Argo observations using machine learning algorithms, *J. Geophys. Res.-Mach. Learn. Comput.*, 1, e2024JH000272, <https://doi.org/10.1029/2024JH000272>, 2024.
- Ito, T., Garcia, H. E., Wang, Z., Cheng, L., Du, J., Roach, C. J., Sharp, J. D., Minobe, S., Zhou, Y., Lu, B., Navarra, G. G., and Bushinsky, S. M.: Assessing the observational uncertainties of dissolved oxygen climatology and seasonal cycle through a coordinated intercomparison project, *Global Biogeochem. Cy.*, 39, e2025GB008751, <https://doi.org/10.1029/2025GB008751>, 2025.
- Keeling, R. F., Körtzinger, A., and Gruber, N.: Ocean Deoxygenation in a Warming world, *Annu. Rev. Mar. Sci.*, 2, 199–229, <https://doi.org/10.1146/annurev.marine.010908.163855>, 2010.
- Koelling, J., Atamanchuk, D., Karstensen, J., Handmann, P., and Wallace, D. W. R.: Oxygen export to the deep ocean following Labrador Sea Water formation, *Biogeosciences*, 19, 437–454, <https://doi.org/10.5194/bg-19-437-2022>, 2022.
- Kwiecek, J. V. and Babbitt, A. R.: A high-resolution atlas of the eastern tropical Pacific oxygen deficient zones, *Global Biogeochem. Cy.*, 35, e2021GB007001, <https://doi.org/10.1029/2021GB007001>, 2021.
- Lauvset, S. K., Key, R. M., Olsen, A., van Heuven, S., Velo, A., Lin, X., Schirnack, C., Kozyr, A., Tanhua, T., Hoppema, M., Jutterström, S., Steinfeldt, R., Jeansson, E., Ishii, M., Perez, F. F., Suzuki, T., and Watelet, S.: A new global interior ocean mapped climatology: the 1° × 1° GLODAP version 2, *Earth Syst. Sci. Data*, 8, 325–340, <https://doi.org/10.5194/essd-8-325-2016>, 2016.
- Levin, L. A.: Manifestation, drivers, and emergence of open ocean deoxygenation, *Annu. Rev. Mar. Sci.*, 10, 229–260, <https://doi.org/10.1146/annurev-marine-121916-063359>, 2018.

- Liu, Q. H., Bao, S. L., Yan, H. Q., Wang, H. Z., and Zhang, R.: Enhancing sea surface salinity short-term prediction using physically informed deep learning, *Appl. Ocean Res.*, 165, 104832, <https://doi.org/10.1016/j.apor.2025.104832>, 2025.
- Lu, B., Zhao, Z., Han, L. Y., Gan, X. Y., Zhou, Y. T., Zhou, L., Fu, L. Y., Wang, X. B., Zhou, C. H., and Zhang, J.: Oxy-Generator: Reconstructing global ocean deoxygenation over a century with deep learning, *Proceedings of the 41st International Conference on Machine Learning*, PMLR 235, 33219–33242, <https://proceedings.mlr.press/v235/lu24n.html> (last access: 8 May 2026), 2024.
- Martin, A. P.: The seasonal smorgasbord of the seas, *Science*, 337, 46–47, <https://doi.org/10.1126/science.1223881>, 2012.
- McDougall, T. J. and Barker, P. M.: Getting started with TEOS-10 and the Gibbs Seawater (GSW) oceanographic toolbox, SCOR/IAPSO WG127, 1–28, ISBN 9780646-55621-5, 2011.
- Mishonov, A. V., Boyer, T. P., Baranova, O. K., Bouchard, C., Cross, S. L., Garcia, H. E., Locarnini, R. A., Paver, C. R., Reagan, J. R., Wang, Z., Seidov, D., Grodsky, A. I., and Beauchamp, J. G.: *World Ocean Database 2023*, edited by: Bouchard, C., NOAA Atlas NESDIS 97, <https://doi.org/10.25923/z885-h264>, 2024.
- Musan, I., Gildor, H., Barkan, E., Smethie Jr., W. M., and Luz, B.: Evidence from dissolved O<sub>2</sub> isotopes in North Atlantic Deep Water for a recent climatic shift, *Geophys. Res. Lett.*, 50, e2022GL100489, <https://doi.org/10.1029/2022GL100489>, 2023.
- Oschlies, A., Duteil, O., Getzlaff, J., Koeve, W., Landolfi, A., and Schmidtko, S.: Patterns of deoxygenation: sensitivity to natural and anthropogenic drivers, *Philos. T. R. Soc. A*, 375, 20160325, <https://doi.org/10.1098/rsta.2016.0325>, 2017.
- Oschlies, A., Brandt, P., Stramma, L., and Schmidtko, S.: Drivers and mechanisms of ocean deoxygenation, *Nat. Geosci.*, 11, 467–473, <https://doi.org/10.1038/s41561-018-0152-2>, 2018.
- Roach, C. J. and Bindoff, N. L.: Developing a New Oxygen Atlas of the World's Oceans Using Data Interpolating Variational Analysis, *J. Atmos. Ocean. Tech.*, 40, 1475–1491, <https://doi.org/10.1175/JTECH-D-23-0007.1>, 2023.
- Ruhl, H. A., Huffard, C. L., Messié, M., Connolly, T. P., Soltwedel, T., Wenzhöfer, F., Johnson, R. J., Bates, N. R., Hartman, S., Flohr, A., Mawji, E. W., Karl, D. M., Potemra, J., Santiago-Mandujano, F., Ross, T., and Smith, K. L.: Decadal change in deep-ocean dissolved oxygen in the North Atlantic Ocean and North Pacific Ocean, *Deep-Sea Res. Pt. I*, 223, 104534, <https://doi.org/10.1016/j.dsr.2025.104534>, 2025.
- Schmidtko, S., Stramma, L., and Visbeck, M.: Decline in global oceanic oxygen content during the past five decades, *Nature*, 542, 335–339, <https://doi.org/10.1038/nature21399>, 2017.
- Sharp, J. D., Fassbender, A. J., Carter, B. R., Johnson, G. C., Schultz, C., and Dunne, J. P.: GOBAI-O<sub>2</sub>: temporally and spatially resolved fields of ocean interior dissolved oxygen over nearly 2 decades, *Earth Syst. Sci. Data*, 15, 4481–4518, <https://doi.org/10.5194/essd-15-4481-2023>, 2023.
- Stramma, L. and Schmidtko, S.: Spatial and temporal variability of oceanic oxygen changes and underlying trends, *Atmos.-Ocean*, 59, 122–132, <https://doi.org/10.1080/07055900.2021.1905601>, 2021.
- Stramma, L., Johnson, G. C., Sprintall, J., and Mohrholz, V.: Expanding oxygen-minimum zones in the tropical oceans, *Science*, 320, 655–658, <https://doi.org/10.1126/science.1153847>, 2008.
- Stramma, L., Schmidtko, S., Levin, L. A., and Johnson, G. C.: Ocean oxygen minima expansions and their biological impacts, *Deep-Sea Res. Pt. I*, <https://doi.org/10.1016/j.dsr.2010.01.005>, 2010.
- Tan, Z., von Schuckmann, K., Speich, S., Bopp, L., Zhu, J., and Cheng, L.: Observed large-scale and deep-reaching compound ocean state changes over the past 60 years, *Nat. Clim. Change*, 16, 58–68, <https://doi.org/10.1038/s41558-025-02484-x>, 2026.
- Wang, Z., Garcia, H. E., Boyer, T. P., Reagan, J., and Cebrian, J.: Controlling factors of the climatological annual cycle of the surface mixed layer oxygen content: A global view, *Front. Mar. Sci.*, 9, 1001095, <https://doi.org/10.3389/fmars.2022.1001095>, 2022.
- Zhou, Y., Gong, H., and Zhou, F.: Responses of horizontally expanding oceanic oxygen minimum zones to climate change based on observations, *Geophys. Res. Lett.*, 49, e2022GL097724, <https://doi.org/10.1029/2022GL097724>, 2022.